New constraints on the intraplate stress field of the Amurian plate deduced from light earthquake focal mechanisms

Andreas Barth [a,b] Friedemann Wenzel [b]

[a] *Heidelberg Academy of Sciences and Humanities, Karlstr. 4, 69117 Heidelberg, Germany*

[b] *Geophysical Institute, University of Karlsruhe, Hertzstr. 16, 76187 Karlsruhe, Germany*

Abstract

The Amurian plate plays an important role for the understanding of eastern Asian plate dynamics. Different models of rigid-rotation and relative velocities with respect to adjacent plates have been proposed. As few GPS data and sparse stress observations have been available until today—particularly for the intraplate region—these models have proven hard to confirm or deny. To address this we determine new focal mechanisms for this region and perform a stress inversion for selected parts of the plate in order to provide better constraints on the plate dynamics.

Most strong earthquakes occur on active plate margins and for these events focal mechanisms are routinely calculated by moment tensor inversion using teleseismic data on a global scale. Away from the plate margins, earthquake magnitudes are smaller and the efficiency of such automated procedures strongly depends on the number of seismic records available. Using the Frequency Sensitive Moment Tensor Inversion allows us to determine source mechanisms of light events with a smaller number of data. For the Amurian plate interior, we calculate 41 focal mechanisms for crustal earthquakes from 1993 to 2008 ($3.9 \leq M_W \leq 5.4$). We combine these data with additional solutions from the literature to perform formal stress inversions for three separate regions. The reliability of the resulting stress orientations is evaluated by bootstrap analysis to show the variability of the principle stress axes.

For all regions the resulting stress field shows a dominant strike-slip regime with an ENE-WSW orientation of the maximum horizontal compressional stress S_H and is consistent with borehole stress data from the World Stress Map at the margins and in the central part of the Amurian plate. Moreover, our analysis reveals differences in both the stress ratio and the S_H orientation within the plate interior. While the northern part of the Amurian plate might be influenced by the Baikal rift in terms of a small anti-clockwise rotation of S_H, the eastern part of the plate clearly responds to the far field plate-boundary forces from the subducting Pacific plate.

Key words: Amurian plate, stress inversion, moment tensor inversion, focal mechanisms, NE China, Russian Far East, eastern Mongolia

1 Introduction

The Amurian plate is situated between the Eurasian and Pacific plates and spans approximately 2500 km in both the north-south and the east-west directions (Figure 1). It covers the border region of NE China, SE Russia, and eastern Mongolia, the Korean peninsula, the East Sea/Sea of Japan, and parts of southern Japan (Bird, 2003). Since Zonenshain and Savostin (1981) suggested the existence of a distinct Amurian plate, its plate kinematics as well as the location of its plate boundaries have been matters of debate. The most evident boundary between Eurasia and the Amurian plate is the Baikal rift, which is undergoing NW-SE extension of 4 mm/yr (Calais et al., 2003). In the southern part of Amuria, velocities range from 2 mm/yr to 8 mm/yr with respect to stable Eurasia (Wang et al., 2001). Different models for the plate rotation have been presented to explain these observations (Zonenshain and Savostin, 1981; Wei and Seno, 1998; Heki et al., 1999; Sella et al., 2002; Kreemer et al., 2003; Calais et al., 2003). The lack of GPS data and the observation of only small relative velocities has led to great uncertainties in the modelled velocities and rotation poles. Strongly differing location estimates for the rotation pole of Amuria with respect to Eurasia have been obtained by different groups and are located NE of the Baikal rift (Calais et al., 2003; Wei and Seno, 1998) and NE of Japan (Sella et al., 2002; Kreemer et al., 2003) with an anti-clockwise rotation and west of Australia (Heki et al., 1999) with a clockwise rotation. Hence, to date the kinematics of the Amurian plate have not been clarified. Petit and Fournier (2005) used GPS data in combination with earthquake slip data and stress orientations to analyse plate-boundary forces with thin-shell finite element models. They reproduced the recent velocity and stress patterns on the Amurian plate and examined the effects of different boundary conditions, namely these representing body forces with respect to variations in the crustal thickness and the influence of indentation, extrusion and subduction processes at the plate boundaries.

Additional information on the intraplate stress field may improve these kinematic models. In this paper, we perform a stress inversion of earthquake focal mechanism data to obtain a more accurate picture of the Amurian intraplate stress field. For this purpose, we calculate focal mechanism solutions for earthquakes with magnitudes of $M_W \geq 3.9$ using the Frequency Sensitive Moment Tensor Inversion (FMTI, Barth et al., 2007), that have not been determined before.

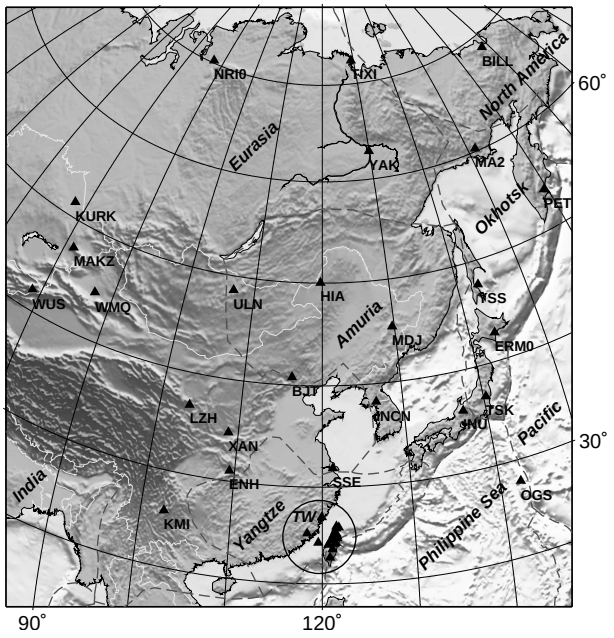

Fig. 1. Distribution of seismometers used in this work. The circle indicates the seismic stations of the Broadband Array in Taiwan for Seismology (network code TW), including stations ANPB, HGSD, HWAB, KMNB, MATB, NACB, PHUB, SSLB, TATO, TDCB, TPUB, TWGB, TWKB, WFSB, YHNB, and YULB. Dashed lines indicate plate boundaries (Bird, 2003).

2 Previous stress analyses

Stress information of regions within plate interiors is rare because of the lack of earthquake source mechanisms. Focal mechanisms on a global scale are provided, for example, by the Global (formerly Harvard) CMT Project or the National Earthquake Information Center (NEIC). These catalogues are globally complete for magnitudes higher than M_W 5.5 (Arvidsson and Ekström, 1998). Local agencies often perform first-motion analyses using local seismometer networks and are able to determine mechanisms for magnitudes below M_W 4.5. To extract stress information from focal mechanism solutions, various approaches have been used. The most suitable method is the formal stress inversion that takes into account the systematic difference between the P-, B-, and T-axis (the principle axes of the moment tensor) and the principle axes of the stress tensor (McKenzie, 1969; Arnold and Townend, 2007; Barth et al., 2008).

Xu et al. (1992) evaluated P-wave first-motion data in common composite solutions for 76 regions in China. Two regions (#1, #2) in NE China lie within our study region and contain a total of 137 earthquakes analysed by Xu et al. (1992). They assigned their stress estimations to B-quality, reflecting the low data coverage and only diffuse clusters of the compiled P-, B-, and T-axes. Both regions show an ENE-WSW orientation of compression in a dominant

strike-slip regime. It was conducted by Xu et al. (1992) that the overall stress field is part of a radial pattern that covers all of China with the minimum horizontal compressional stress S_h lying on curved trajectories centred at the Indian-Eurasian collision zone.

Xu (2001) recompiled stress data from the World Stress Map release 1992 (Zoback, 1992) with additional Harvard-CMT solutions for China. For NE China, borehole data show a maximum horizontal compressional stress S_H oriented ENE-WSW. Xu (2001) concluded that in SE Asia and especially in southern China S_H orientations are not parallel to directions of motion of the Eurasian plate as a whole, but instead are probably affected by smaller plates in that region. A recent study of tectonic stresses in China (Zheng and Chen, 2006) added CMT data to the analysis of Xu (2001) and confirmed the results of the original study.

In addition to these analyses of the intraplate stress field of the Amurian plate, various studies have been performed on its plate margins. In particular, the seismically active zones of the Baikal rift and Japan have been investigated by formal stress inversions of earthquake focal mechanisms (cf. Figure 7). Delvaux et al. (1997) deduced a detailed history of the evolution of the paleo- and present-day stress field. During several phases the stress field in the Baikal rift changed from compressional regimes in a proto-rift stage to strike-slip and pure extensional regimes during active rifting. The present-day stress field shows predominant extension in NW-SE direction in the central part and an ENE-WSW oriented S_H within a transpressional regime in the southwestern part of the rift. Towards the northeast Doser (1991a,b) showed that S_H also rotates to an ENE-WSW orientation. Radziminovich et al. (this volume) confirmed these results by performing stress inversions of recent focal mechanism solutions from first-motion analysis for the Lake Baikal region. For the region southeast of the Baikal (Transbaikal), Radziminovich et al. (this volume) obtained strike-slip and transtensional conditions with S_H oriented NE-SW. Townend and Zoback (2006) performed stress inversions on the eastern margin of the Amurian plate. They studied the relation of the stress and strain pattern and observed a regional rotation of S_H from ENE-WSW in southwestern Japan to WNW-ESE in the northeast.

3 Frequency Sensitive Moment Tensor Inversion

We determine new focal mechanisms of earthquakes within the Amurian plate for the derivation of tectonic stress orientations thereafter. For this purpose, we perform the Frequency Sensitive Moment Tensor Inversion (FMTI) for selected earthquakes using regional and teleseismic waveform data.

3.1 Earthquake selection and waveform data

We determine focal mechanisms by FMTI only for intraplate crustal earthquakes. This enables us to analyse the stress field within the Amurian plate using seismic events that are not directly affected by plate-boundary kinematics. We define corridors along the plate boundaries to select and study only earthquakes within these margins. The definition of the Amurian plate boundary is still a matter of debate. The northwestern boundary is fixed by the Baikal rift zone that extends over a length of 1600 km and separates the Amurian plate from the Siberian platform, which is part of Eurasia. Attached to the Baikal rift system, the Stanovoy foldbelt forms the northern plate boundary (Zonenshain and Savostin, 1981; Heki et al., 1999). However, the exact location of the plate boundary within this >200 km-wide zone is still under discussion. We adopt the model of Bird (2003), who put the plate boundary to the very north of this zone (Figure 2). In the east, the seismic active zones of Sakhalin and Japan define the plate boundary. The existence of the Okhotsk plate, which separates the Amurian plate from the Pacific plate, has not yet been verified (Heki et al., 1999). The western and southern margins, however, are indefinite, because neither distinct fault systems, nor an obvious zone of seismicity exists. For the selection of intraplate earthquakes, we take a conservative attempt including only earthquakes with a distance of at least 130 km to the Amurian plate boundary. Additionally, we exclude all events that are directly related to the Baikal rift zone and focus only on the northern part of the plate, skipping the seismic active region along the coastal line of the East Sea/Sea of Japan and south of it towards the Korean Peninsula.

Earthquake hypocentres and origin times are taken from the Engdahl catalogue of relocated earthquakes when available (Engdahl et al., 1998, Engdahl pers. communication). Additionally, we use bulletins of the International Seismological Centre (ISC), the NEIC, and local bulletins for event locations. We restrict our data selection to events of $m_b \geq 4.0$ occurring later than 1993, to obtain a sufficient coverage of digital broadband seismometers. The application of these criteria results in 147 earthquakes that are shown in Figure 2 together with the seismicity on the plate margins and surrounding regions. We use waveform data from 41 seismometers with source-receiver distances of up to 3330 km (Figure 1). The seismic networks used in our analysis are the Broadband Array in Taiwan for Seismology, the China Digital Seismic Network, GEOSCOPE, the Global Seismograph Network (GSN), the Kazakh Network (IGR, NNC), the New China Digital Seismic Network, and the Ocean Hemisphere Network (part of Pacific21).

3.2 Method

We use the semi-automatic Frequency Sensitive Moment Tensor Inversion (FMTI) to determine the full moment tensor of the 147 selected events (Barth et al., 2007). This method automatically determines the frequency band in which the best fit to the seismic waveforms can be obtained. It is based on a damped least squares moment tensor inversion in the frequency-domain that accounts for both phase and amplitude radiation pattern (Giardini, 1992). For each event-seismometer combination, an individual re-alignment in the time-domain is calculated for vertically polarised waves (Rayleigh- and P/SV-waves) and horizontally polarised waves (Love and SH-waves). We use discrete crustal focal depths (6, 10, 14, 18, 25, and 33 km) to determine a minimum variance solution. Normal mode summation (Woodhouse, 1988) based on the PREM 1D earth model (Dziewonski and Anderson, 1981) is used to generate synthetic waveforms for frequencies lower than 29 mHz (periods longer than 34.5 s). Higher frequencies, however, are strongly influenced by crustal structure, due to their shorter wavelengths and thus cannot be modelled by a one dimensional earth model (Larson and Ekström, 2001; Šílený, 2004). The upper period limit is about 100 s, since light earthquakes are recorded at teleseismic distances only below a period of 100 s with amplitudes higher than the seismic noise level (Barth et al., 2007). Our data processing automatically chooses waveform data with a sufficient signal-to-noise ratio by evaluating the data variance ε (Barth et al., 2007). The variance ε between observed $\mathbf{d}$ and synthetic waveforms $\mathbf{s}$ in the frequency domain is calculated by:

$$\varepsilon = \frac{(\mathbf{d} - \mathbf{s})^2}{\mathbf{d}^2}, \tag{1}$$

We perform the FMTI for discrete focal depths and 8 mHz-wide frequency pass bands. The depth-frequency pair with the lowest variance ε and consistent focal planes for neighbouring frequency bands is selected. Details of the data processing can be found in Barth et al. (2007).

3.3 Results

We determine focal mechanisms for 41 of the 147 selected earthquakes. Only for these events the quality criteria are fulfilled for at least six waveform components (for details see Barth et al., 2007). The main reasons that the remaining events do not meet the criteria are too noisy data, due to low moment magnitudes M_W, and too few available waveform data. The results of the FMTI are given in Table 1 and Figure 2. The events are grouped in three major clusters of seismicity within the study region. The predominant regime

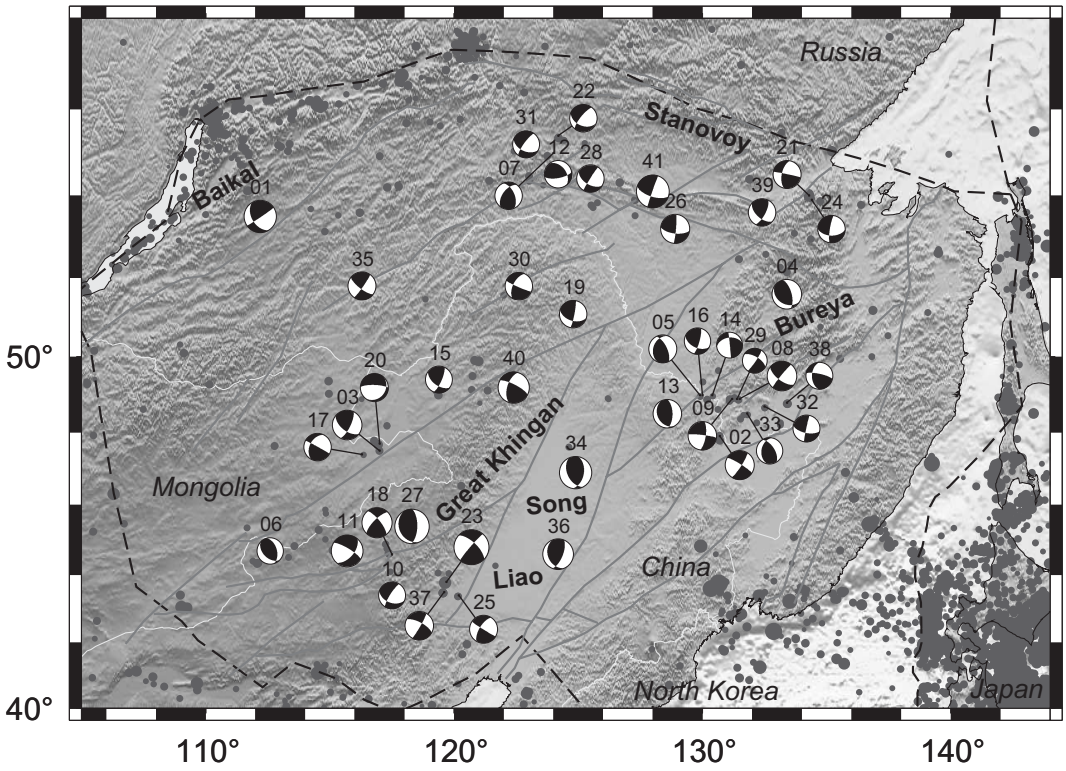

Fig. 2. Focal mechanisms determined by the Frequency Sensitive Moment Tensor Inversion in this work and additional earthquakes (grey dots, data by ISC, NEIC and additional agencies 1993–2008, $m_b \geq 3.0$). Numbers identify the events as given in Table 1. Solid lines represent the main fault systems in the study region (Şengör and Natal'in, 1996). Dashed lines indicate plate boundaries (Bird, 2003).

is strike-slip faulting with locally differing characteristics. One cluster is located in the Stanovoy foldbelt at the northern margin of the Amurian plate. Here we observe normal faulting components especially in the west towards the Baikal rift zone (earthquakes number #22, #31). This is likely related to the apparent extension of the Baikal rift. However, we also determine two thrusting events (#07, #39). Another concentrated region of seismic activity is found in the Bureya (Bureinskij) mountain range southeast of the Stanovoy belt. In addition to right-lateral strike-slip on the NE-SW oriented major fault systems, we find three thrust events striking in northerly directions (#05, #13, #33). The Song Liao basin separates the Bureya mountains from the Great Khingan (Da Hinggan Ling) mountain range (Figure 2). Whereas the basin itself only exhibits minor seismicity including two pure thrusting mechanisms (#34, #36), the Great Khingan has a higher activity. In the Great Khingan we observe a heterogeneous distribution of strike-slip mechanisms with partly normal and partly thrusting portions.

The overall azimuthal distributions of the waveforms used are good for most of the 41 newly determined focal mechanism solutions. For some earthquakes, however, there is a lack of data from the east and northeast. The moment

Table 1
Results of the Frequency Sensitive Moment Tensor Inversion

nr	date	time	lat	lon	d	M_W	ϕ	δ	λ	N	ε	F	DC
1	1993-09-05	21:49:47	53.5	112.2	33	5.0	148	47	3	11	0.35	16-27	75
2	1993-10-01	22:40:10	47.9	130.7	25	4.5	33	81	-172	6	0.56	18-29	82
3	1993-11-19	20:31:47	47.5	117.0	33	4.5	128	57	20	7	0.68	17-28	52
4	1994-05-05	03:36:35	51.6	133.4	18	4.5	122	32	52	7	0.47	15-29	56
5	1994-06-04	19:36:11	49.0	129.9	25	4.3	200	33	131	10	0.56	19-29	92
6	1996-05-04	07:01:34	44.7	112.6	14	4.1	135	44	69	7	0.56	16-29	71
7	1997-11-10	17:47:24	55.0	124.0	25	4.2	217	54	136	12	0.51	19-27	64
8	1998-07-24	23:12:17	48.9	131.5	25	4.6	127	65	-5	20	0.46	20-29	85
9	1998-07-24	23:19:39	48.9	131.2	10	4.4	9	71	-174	6	0.17	17-29	78
10	1998-12-19	06:09:17	43.4	117.5	25	4.2	111	45	-15	11	0.41	18-27	82
11	1999-01-29	05:44:26	44.7	115.7	10	4.9	40	55	-164	23	0.29	18-27	59
12	1999-04-25	22:20:17	54.5	124.2	25	4.3	325	42	149	9	0.52	16-28	92
13	1999-08-13	18:36:25	48.5	128.6	14	4.4	152	29	66	26	0.32	21-29	66
14	1999-09-03	11:23:32	49.0	130.4	14	4.0	263	41	-1	8	0.60	18-28	47
15	2000-02-02	17:04:52	49.4	119.4	18	4.2	125	54	17	10	0.38	19-29	59
16	2000-05-14	15:48:53	49.0	130.0	10	4.1	115	50	14	12	0.54	17-28	60
17	2000-12-30	23:10:24	47.4	116.3	18	4.2	207	43	177	10	0.36	17-26	41
18	2002-10-20	15:46:18	44.6	117.5	10	4.7	225	72	162	44	0.32	16-25	44
19	2002-12-08	20:54:15	51.1	124.8	18	4.3	107	48	8	12	0.38	20-29	14
20	2003-06-18	14:24:32	47.7	117.0	18	4.4	35	22	-144	16	0.50	15-29	17
21	2003-07-18	14:03:09	54.0	134.3	33	4.3	192	60	178	14	0.43	16-28	91
22	2003-07-30	04:30:50	55.4	124.2	25	4.2	114	43	-21	6	0.47	18-29	68
23	2003-08-16	10:58:44	43.8	119.7	33	5.4	313	66	4	56	0.21	14-24	79
24	2003-10-16	21:19:20	53.9	134.4	18	4.3	91	51	-11	13	0.40	21-29	71
25	2003-10-17	01:38:31	43.4	120.2	33	4.3	212	65	-178	9	0.30	20-29	54
26	2004-01-25	19:46:27	53.2	128.9	18	4.5	97	65	5	36	0.38	19-29	96
27	2004-03-24	01:53:48	45.4	118.3	25	5.4	157	27	68	55	0.28	19-29	25
28	2004-03-24	19:55:50	54.4	125.5	25	4.2	120	53	-3	10	0.35	17-29	87
29	2005-01-15	02:54:50	48.9	131.4	14	3.9	300	63	-8	6	0.56	20-29	11
30	2005-01-24	12:22:46	51.8	122.6	25	4.3	207	57	-173	13	0.40	17-29	61
31	2005-02-12	17:19:04	55.2	122.9	14	4.2	114	47	-17	11	0.42	20-29	61
32	2005-03-23	02:13:05	48.7	132.5	6	4.2	101	63	-3	20	0.48	20-29	73
33	2005-07-06	23:10:14	48.5	131.8	10	4.1	191	39	127	9	0.61	16-26	74
34	2005-07-25	15:43:35	46.9	124.9	10	5.0	154	47	63	45	0.27	18-28	72
35	2006-01-06	01:56:38	51.8	116.3	10	4.4	127	73	5	7	0.16	17-29	66
36	2006-03-31	12:23:17	44.6	124.2	6	4.7	156	32	48	17	0.31	17-27	27
37	2006-11-03	06:21:39	43.5	119.6	18	4.4	298	69	-5	19	0.38	19-29	49
38	2007-04-22	10:04:00	48.8	133.4	25	4.2	180	46	162	10	0.34	19-29	38
39	2007-09-15	20:56:18	53.6	132.4	25	4.2	132	56	24	6	0.30	20-29	83
40	2008-06-10	06:05:02	49.2	122.4	18	4.9	198	57	162	9	0.45	20-29	88
41	2008-06-17	17:26:12	54.1	128.0	25	5.1	108	64	-1	23	0.27	8-28	94

Columns as follows: number of event, date and time of occurrence [yr-mo-day, hh:mm:ss], latitude, longitude, depth d [km], moment magnitude M_W, strike ϕ, dip δ, rake λ, number of inverted waveform components N, variance ε (Equation 1), inverted frequency range F [mHz], and percentage of double couple DC.

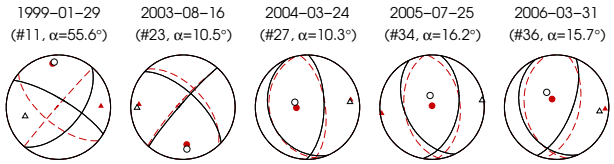

Fig. 3. Comparison of the focal mechanism solutions calculated by CMT (red, dashed nodal planes and filled symbols) and the FMTI (black, solid nodal planes and open symbols). Triangles indicate P-axes, circles indicate T-axes. Only the pure DC part is shown. Minimum rotation angles α between the CMT and the FMTI solutions are calculated after Walsh et al. (2009).

magnitudes M_W range from 3.9 to 5.4 with a mean data variance of $\bar{\varepsilon} = 0.41 \pm 0.10$. On average, 16 waveform components are inverted for the moment tensor. The mean value for the double couple percentages is $\bar{DC} = 63.5\% \pm 18.0\%$. Moment tensors with a low double couple part (six solutions with $DC < 40\%$) may result from inconsistent data or random noise (Kuge and Lay, 1994; Henry et al., 2002). Barth (2007) showed that low DC parts are often unrelated to the shape of the pure double couple mechanism. The average lower frequency of the automatically determined pass band is 17.7 mHz, corresponding to an upper period of 56.5 s. Combined with the constant lower period limit of 34.5 s (29 mHz), this results in a very narrow pass band that has a high signal-to-noise ratio and thus is adequate for the moment tensor inversion of light earthquakes.

Eight focal mechanisms calculated by the Global (formerly Harvard) CMT Project are available for our study region. For those events that took place since 1993, we also determine the focal mechanism by using the FMTI (#11, #23, #27, #34, #36). Their magnitudes range from M_W 4.7 to M_W 5.4. All but event #11 show very similar source mechanisms and same magnitudes compared to the corresponding CMT solutions (Figure 3). The minimum rotation angles α (Walsh et al., 2009) between the CMT and our FMTI solutions range from 10.3° to 16.2°. The event on 29 January 1999 (FMTI: M_W 4.9, CMT: M_W 5.0), however, shows very similar striking nodal planes and T-axes for both solutions, but obvious variations in plunge ($\alpha = 55.6°$). This difference might be due to the fact that CMT uses only 12 waveform components for inversion, while our dataset consists of 23 traces (cf. Table 1). For a M_W 4.6 earthquake on 19 September 2005, no stable focal mechanism can be determined.

3.4 The 24 March 2004 M_W 4.2 earthquake

A representative example in terms of data quantity, quality and waveform fit is the 24 March 2004 (19:55 UTC) M_W 4.2 earthquake that occurred on the southern margin of the Stanovoy foldbelt (event number #28). Six seis-

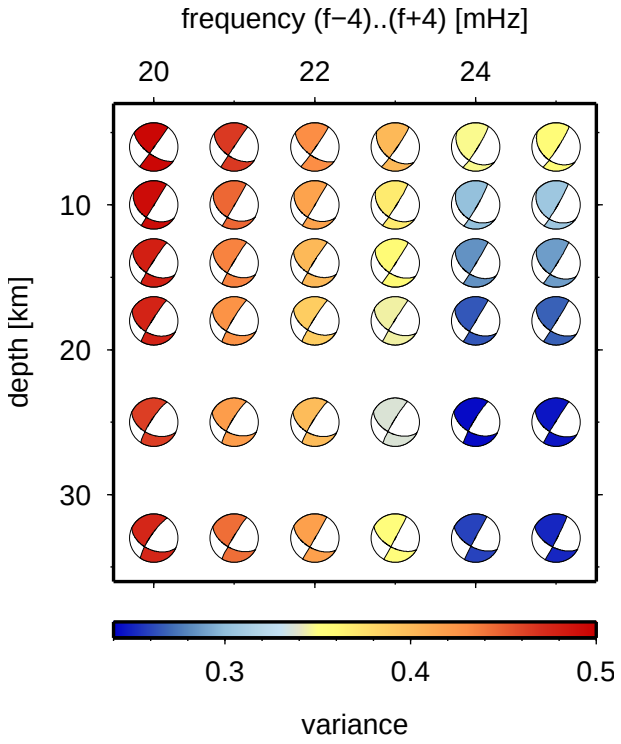

Fig. 4. Frequency sensitive moment tensor inversion of the 24 March 2004 (19:55 UTC) M_W 4.2 event. Inversion results are shown for different combinations of discrete hypocentral depths and 8 mHz-wide frequency pass-bands, coloured by variance ε. Annotations correspond to the mid-frequency of each pass-band.

mometers with a maximum distance of 1900 km to the epicentre are used for the FMTI. Figure 4 shows the result of the FMTI for different frequency pass-bands and discrete source depths. The depth-frequency combination with lowest variance is found at f =21–29 mHz for a source depth $d = 25$ km. The focal mechanism is stable for all pass-bands above 16–24 mHz with increasing variances at lower frequency. This is mainly due to the lower signal-to-noise ratio at lower frequencies for light events at teleseismic distances, compared to higher frequencies. Also, the source mechanism we obtain varies only slightly with depths. Only for a hypocentral depth of 6 km some focal mechanisms show obvious deviations from the minimum variance solution. We perform the final inversion for the extended frequency pass band of f =17–29 mHz for which the focal mechanism is stable in combination with a low data variance (Figure 5). The final solution shows a strike-slip mechanism with a magnitude of M_W 4.2 and a data variance of $\varepsilon = 0.35$. The stress inversion for the Stanovoy foldbelt determines the vertical NE-SW striking nodal plane as fault plane with a misfit angle of $\beta(\#28)_{bin2} = 9.1°$ that is below the average of $\bar{\beta}(bin2) = 15.0°$ for the inverted focal mechanisms (see paragraphs 4.2, 4.3, and Table 3).

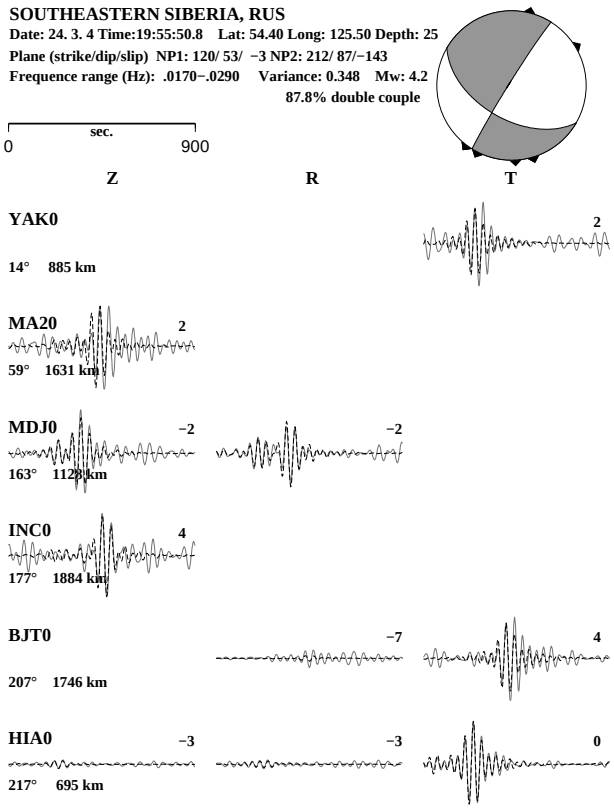

Fig. 5. Inversion result of the 24 March 2004 (19:55 UTC) M_W 4.2 event. Triangles around the focal mechanism indicate station azimuth. The inverted waveform traces on the vertical, radial and transversal component (Z, R, T) are plotted as grey solid lines, synthetics as black dashed lines. Station name and time-shift in seconds is given above each trace, azimuth and epicentral distance below. Amplitudes are plotted normalised to the maximum of each station.

4 Stress inversion

We use the new and existing earthquake focal mechanism determinations to analyse the intraplate stress field of the Amurian plate via formal stress inversion. This provides additional information on the intraplate stress field that may improve kinematic models for the Amurian plate and thus improve the understanding of the regional tectonics.

4.1 Focal mechanism data

For the stress inversion, we combine the 41 new focal mechanisms determined in this study with additional data from the literature (Table 2). Seven mechanisms in the Stanovoy foldbelt and south of it are taken from Parfenov et al. (1987) and four mechanisms from Wang and Xu (1986) in the Great Khin-

Table 2
Additional focal mechanisms used for stress inversion

nr	date	time	lat	lon	d	M	ϕ	δ	λ	source
42	1960-04-13	07:57	44.7	126.9	8	M_S 5.7	318	48	-10	W+X86
43	1963-06-21	13:44	47.9	130.6	C	M_S 5.8	104	74	-10	W+X86
44	1966-10-02	02:24	43.8	125.1	10	M_S 5.2	42	64	156	W+X86
45	1970-08-29	14:59	51.1	135.3	14	M_S 5.2	188	39	32	P87
46	1972-06-13	10:45	54.3	126.5	10	M_S 5.7	25	80	-179	P87
47	1973-11-02	07:31	54.4	125.4	7	M_S 5.5	247	35	-20	P87
48	1975-06-29	12:24	53.6	132.2	12	M_S 5.1	132	24	96	P87
49	1976-08-28	16:23	43.9	114.2	C	M_S 5.3	286	59	-17	W+X86
50	1976-11-24	xx:xx	54.1	122.0	18	M_S 5.0	316	21	141	P87
51	1977-08-16	13:56	54.2	128.9	13	M_S 5.1	110	84	0	P87
52	1978-08-21	xx:xx	55.2	124.8	10	M_S 4.0	112	27	90	P87
53	1980-02-10	04:46	48.7	121.0	15	M_W 5.1	130	54	6	CMT
54	1986-08-15	20:20	48.6	126.1	15	M_W 5.0	116	63	-12	CMT

Columns as follows: number of event, date and time of occurrence [yr-mo-day, hh:mm], latitude, longitude, depth d [km] (C indicates crustal hypocentre), magnitude M, strike ϕ, dip δ, rake λ, and data source (W+X86: Wang and Xu (1986), P87: Parfenov et al. (1987)).

gan mountain range, the Bureya mountains, and the Song Liao basin. Both first-motion analyses only cover the time before 1980. The calculation of additional high quality first-motion focal mechanisms of earthquakes $M_W < 4.0$ would be desirable and could supplement the stress field analysis. We add the only two CMT solutions available for Amuria from before 1993 (Khingan and Song Liao). In total we use 54 focal mechanisms for the stress analysis divided into three spatially separated groups. The bins are arranged according to the overall tectonic setting and the seismicity pattern. Bin 1 (Khingan) covers the region between Lake Baikal in the west and the Song Liao basin in the east. It is dominated by the NE-SW striking Altaid fault systems and the Great Khingan mountain range (Şengör and Natal'in, 1996) (cf. Figure 2). At the northern plate margin of the Amurian plate, bin 2 (Stanovoy) contains the earthquakes of the Stanovoy foldbelt. East of it, bin 3 (Bureya) is located in the Manchuride crystalline blocks forming the Bureya mountain range.

4.2 Method

The formal stress inversion from focal mechanisms is based on two basic assumptions for the study region (Michael, 1984): (a) The stress field is uniform and invariant in space and time. (b) Earthquake slip occurs in direction of maximum shear stress (Wallace-Bott hypothesis, Bott, 1959).

To take into account the ambiguity between focal and auxiliary planes of the

source mechanism, we invert both nodal planes as if they were independent data. In a second step the worse fitted auxiliary planes are removed and the inversion is performed again. To linearise the inversion, it is assumed that similar magnitudes of shear stress are present on each inverted fault. Hence, the inversion after Michael minimises for both, (a) the angle between slip direction and the direction of maximum shear stress—denoted as misfit angle β on one hand and (b) the deviation of the normalised shear stress magnitudes $|\tau|$ from the reference value $|\tau_0| = 1$ on the other hand (Michael, 1984). A comparison of this method and the stress inversion program TENSOR (Delvaux and Sperner, 2003) is found in Delvaux and Barth (submitted). They show that results of the stress inversion are nearly independent of the inversion technique.

For the calculation of confidence regions for the principle stress axes a statistical approach is applied, which inverts different combinations of fault planes out of the original dataset, to see which stress tensor is most likely. For this purpose, the composition of each new dataset is twofold: First a bootstrap routine is performed that picks n mechanisms at random from the original n events. Each new dataset then will have some mechanisms repeated twice or more times. Thereafter the fault plane is chosen randomly from the two auxiliary planes (Michael, 1987). Thus, at a time 5000 synthetic datasets are compiled from one original set of focal mechanisms and inverted for the stress tensor. The analysis of the resulting stress tensors gives confidence regions that contain 95% and 50% of the principle stress axes, respectively, and are mapped in a stereonet projection. For the final visualisation, the exact orientations of the horizontal stress axes (S_H and S_h) are computed with the formula of Lund and Townend (2007).

4.3 Results

We calculate the stress tensor and misfit angles β for the bins defined above and additionally study the influence of changing the bin boundaries. For this latter purpose, we extend the bins onto the transition zones between them that include earthquakes that cannot be assigned clearly to one of the original bins. First, between bin 1 and bin 3 these are events #34, #36, #42, #44, and #54 in the Song Liao basin and east of it (transition A, cf. Tables 1 and 2). Two of the events show a thrusting mechanism, while the others are mainly strike-slip events (#44 with a high thrusting component). Secondly, between bin 2 and bin 3 events #04 and #45 clearly lie south of the Stanovoy foldbelt but in a distance of more than 200 km north of the earthquake cluster of bin 3 (transition B).

The results of the stress inversions are summarised in Table 3. Two focal

Table 3
Stress inversion results

bin	location	S_H [°]	N	R	β [°]	$\Delta\beta$ [°]	$\lvert\bar{\tau}\rvert$	$\Delta\lvert\bar{\tau}\rvert$	Q
1	Khingan	74.1	19	0.49	8.5	5.8	0.95	0.19	A
1+A	Khingan	77.7	24	0.47	11.6	9.7	0.93	0.19	
2	Stanovoy	59.1	15	0.47	15.0	8.0	0.93	0.17	B
2+B	Stanovoy	67.7	17	0.47	17.9	14.7	0.89	0.21	
3	Bureya	70.2	11	0.40	12.2	7.5	0.94	0.16	B
3+A	Bureya	78.0	16	0.27	15.4	11.5	0.93	0.12	
3+B	Bureya	75.1	13	0.31	18.9	23.8	0.88	0.12	

Columns as follows: bin number, location, direction of maximum horizontal compressional stress S_H clockwise from north, number of inverted focal mechanisms N, stress regime R, average misfit angle $\bar{\beta}$ and standard deviation $\Delta\bar{\beta}$, average normalised shear stress amplitude $|\bar{\tau}|$, standard deviation $\Delta|\bar{\tau}|$, and quality Q.

mechanisms have been excluded, since they result in high misfit angles β. Event #47 occurred on 02 November 1973 and is located in the Stanovoy foldbelt. Within bin 2 its misfit angle is $\beta(\#47)_{bin2} = 96°$. The second event (#14), which occurred on 03 September 1999 in the Bureya mountains, gives a misfit of $\beta(\#14)_{bin3} = 42°$. After excluding both solutions misfit angles for the remaining focal mechanisms are below 32°. Two arguments might explain high misfit angles: Either an earthquake does not react as a consequence of the surrounding regional stress field and is mainly driven by local forces or the fault plane solution has uncertainties in the orientation of the nodal planes. Michael (1991) showed by synthetic tests that standard deviations of 15° in the orientation of the fault planes can result in an average misfit angle $\bar{\beta} \approx 43°$.

The incorporation of transition zone A (Song Liao basin) results in an increase of the average misfit angle $\bar{\beta}$ for both adjacent bins 1 and 3 of 3.1° and 3.2°, respectively. Both values are smaller than the standard deviation $\Delta\bar{\beta}$. Moreover, transition zone A forces a clockwise rotation of S_H for both bins ($S_H(bin1 + A) - S_H(bin1) = 3.6°$ and $S_H(bin3 + A) - S_H(bin3) = 7.8°$), slightly indicating a local stress change within the basin. Because of the apparent tectonic difference to the neighbouring regions and this tendency, we do not include transition zone A into the inversion. A separate stress inversion for the Song Liao basin is not possible, since the number of focal mechanism data is not sufficient. Transition B consists of only two events, but increases the misfit angle for bin 2 and bin 3 clearly by 2.9° and 6.7°, respectively. The event responsible for this result is the M_S 5.2 earthquake on 29 August 1970 (#45), that for both bins shows the highest misfit between slip direction and direction of maximum shear stress ($\beta(\#45)_{bin2+B} = 63°$ and $\beta(\#45)_{bin3+B} = 83°$). Again, this might be due to the influence of the local stress field or uncertainties in the fault plane solution. Because of this obvious misfit, we also exclude transition zone B. In general, including the two transition zones results in a decrease of the average normalised shear stress amplitude $|\bar{\tau}|$ and thus also confirms the inconsistency of the additional focal mechanisms with the original

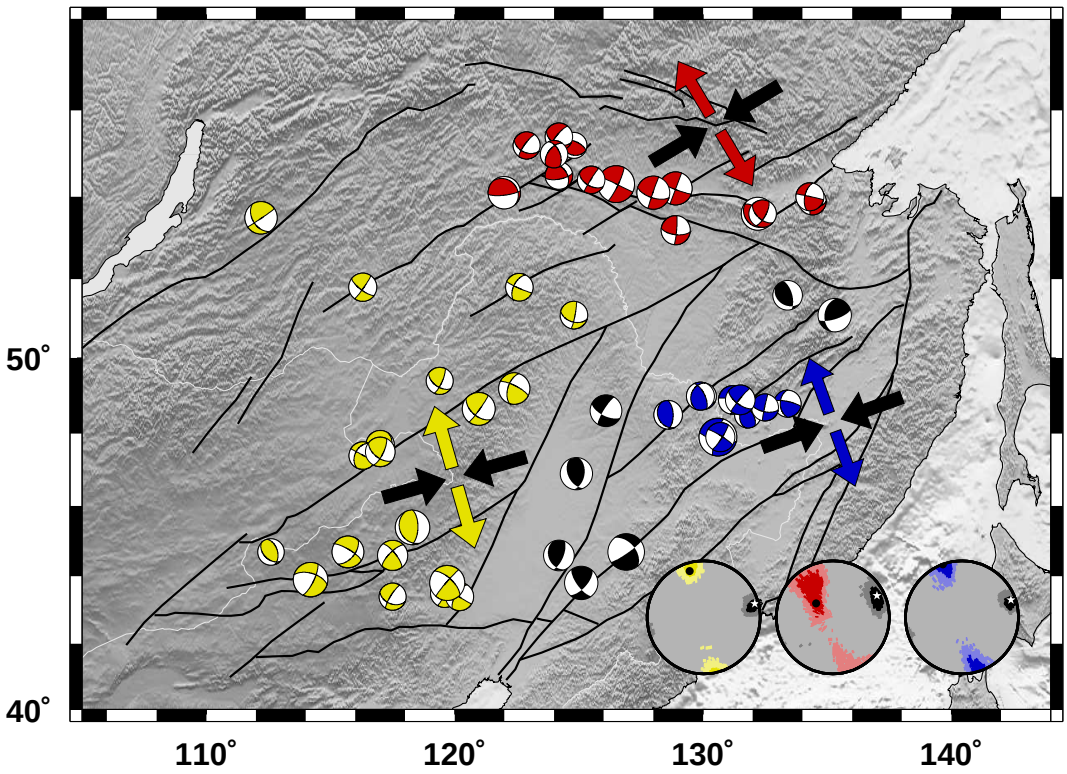

Fig. 6. Formal stress inversion of focal mechanisms determined in this study combined with additional solutions. Colours indicate the three separate inversion bins (yellow: bin 1 (Khingan), red: bin 2 (Stanovoy), blue: bin 3 (Bureya)). Vectors give the orientations of maximum and minimum horizontal compressional stress S_H and S_h, respectively. Vector lengths are scaled by stress ratio R. The equal-area stereonets on the lower right show the confidence regions for the orientation of the principle stress axes σ_1 (black) and σ_3 (coloured) for each stress inversion. Bright colours indicate regions of 50% confidence, while pale colours indicate the 95% regions. The final orientation of σ_1 and σ_3 is shown by a white star and a black dot, respectively.

data (Michael, 1984).

Excluding both transition zones, our stress inversion results in stress orientations for the three original bins (Figure 6). Bin 1 in the Great Khingan mountain range and adjacent regions shows an ENE-WSW oriented maximum horizontal compressional stress $S_H(bin1) = 74.1°$. With $N(bin1) = 19$ inverted focal mechanisms and an average misfit angle of $\bar{\beta}(bin1) = 8.5°$ it meets the World-Stress-Map (WSM) criteria for FMF A quality (i. e., S_H within $\pm 15°$, Heidbach et al., this volume). $|\bar{\tau}(bin1)|$ deviates only little from one, supporting the consistency of the focal mechanism data. The stress ratio R (Bott, 1959)

$$R = \frac{\sigma_2 - \sigma_3}{\sigma_1 - \sigma_3} \tag{2}$$

describes the ratio of the principle stress magnitudes and ranges between zero and one. The inversion of bin 1 gives a value of $R(bin1) = 0.49$ that, in combination with a sub-horizontal σ_1- and σ_3-axis, indicates a pure strike-slip stress regime. The statistical bootstrap analysis for the estimation of confidence regions shows a stable orientation of the principle stress axes σ_1 and σ_3 (Figure 6). The prevailing majority of solutions varies only little in plunge and lies within an azimuthal range of approximately $\pm 13°$ (95% confidence region), which is very similar to the WSM A quality criterion. A further subdivision of the bin does not reveal any significant changes.

For the Stanovoy foldbelt (bin 2) the stress inversion results in an orientation of maximum compression $S_H(bin2) = 59.1°$ that is an anti-clockwise rotation of 15° compared to bin 1. The assigned quality is B (i. e., S_H within $\pm 20°$, $N(bin2) = 15$, $\bar{\beta}(bin2) = 15.0°$). Accordingly, the 95% confidence regions show an azimuthal location of σ_1 and σ_3 of around $\pm 20°$. Although the best-fit σ_3-axis has a steep plunge indicating predominantly thrust faulting, the large confidence regions cover the area of strike-slip regime to the greater part (cf. Figure 6). This ambiguous result of the bootstrap analysis indicates a strong influence of single fault plane solutions that turn the regime to either thrust faulting or strike-slip. A further subdivision of the bin is not possible due to the low number of focal mechanisms.

The third region that is inverted for the stress field is located in the southern Bureya mountains (bin 3). With $S_H(bin3) = 70.2°$ the orientation is similar to bin 1 west of it. However, the sub-horizontal σ_1- and σ_3-axis and a stress ratio $R(bin3) = 0.40$ describes a transpressional regime. The data quality is B ($N(bin3) = 11$, $\bar{\beta}(bin3) = 12.2°$) and the confidence regions support the compressional component of the stress field by a compact clustering of the σ_1-axis comparable to bin 1, but a σ_3-axis with a more variable plunge.

5 Discussion

Our stress inversion results show a predominant strike-slip regime with a NE-SW to ENE-WSW oriented maximum horizontal compression S_H. The tertiary fault system striking mostly NE-SW is activated generally with right-lateral shear-slip. Thus, to first order, the Amurian plate is characterised by a homogeneous intraplate stress field as far as the orientation of stress is concerned, which is in agreement with the analysis of the global stress pattern of Heidbach et al. (this volume) who show large spatial wavelengths for stress pattern changes in that region.

However, we find differences both in the S_H orientation and the stress ratio between the three bins: The largest deviation of S_H results for the Stanovoy

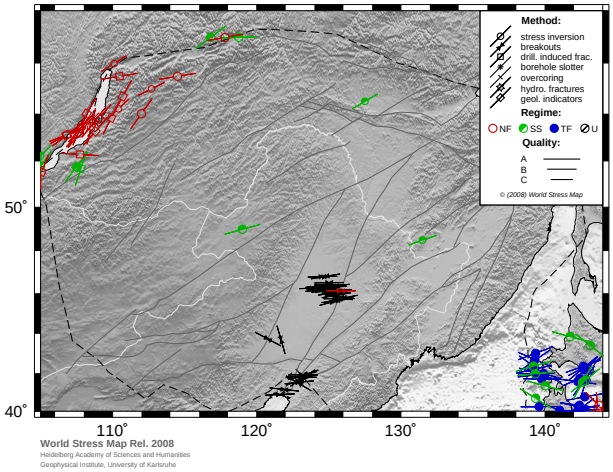

Fig. 7. Orientations of maximum horizontal compressional stress S_H. The three data points with strike-slip regime in the centre of the Amurian plate result from our study. Other data is taken from the WSM stress data release 2008 (Heidbach et al., this volume, single focal mechanisms excluded).

foldbelt compared to the other two regions. In this northern part of Amuria $S_H(bin2)$ is oriented N59°E, while south of it S_H is N74°E and N70°E for bins 1 and 3, respectively (Table 3). The rather large confidence regions allow to interpret the stress field as a strike-slip or predominantly thrust faulting regime. This result might be explained by an influence of the compressional regime of the Pacific subduction on at least parts of the Stanovoy foldbelt. The S_H orientation is probably related to NE-SW orientation of S_H with normal faulting regimes along the main Baikal rift (Delvaux et al., 1997, incorporated in the World-Stress-Map (WSM) 2008 release (Heidbach et al., this volume), Figure 7).

The easternmost region of the work of Radziminovich et al. (this volume) directly connects to the western margin of our study region. They report strike-slip and transtensional conditions with S_H oriented in NE-SW. Since the Great Khingan mountain range region (bin 1) shows a pure strike-slip regime with S_H oriented in ENE-WSW directions, there is a slight change of regime. This is probably due to the decreasing influence of the active Baikal rift that is also apparent in the region northeast of the Baikal sea with S_H oriented ENE-WSW (Doser, 1991a,b). Within the Song Liao basin and on faults parallel to its NE-SW striking structure we observe thrust faulting mechanisms. The incorporation of focal mechanisms from the basin (transition A) to the stress inversion results in a clockwise rotation of S_H towards E-W orientation (Table 3). This is consistent with stress data from borehole breakout analyses (WSM 2008 release). Those data show a N85°E trending S_H for the basin that reveals a slight local stress rotation due to the local basin tectonics (Figure 7).

The transpressional regime in the eastern part of Amuria (bin 3) is most likely

influenced by the plate-boundary forces of the subducting Pacific plate at the Kuril trench and northern Japan. Thus it can be seen as a transition from the strike-slip dominated plate interior to the compressive regime with S_H oriented WNW-ESE in northern Japan (Figure 7, Townend and Zoback, 2006).

6 Conclusions

We successfully use the Frequency Sensitive Moment Tensor Inversion method (FMTI) to determine 41 new moment tensors of light earthquakes with magnitudes as low as M_W 3.9 using regional and teleseismic waveform data. This allows us to perform a formal inversion for the intraplate stress field orientations for three spatially separated bins. Thus, we are able to draw a differentiated picture of the Amurian plate stress field. Our new data describe a strike-slip regime with an NE-SW to ENE-WSW orientation of S_H that might be influenced by the Baikal rift extension only in a small anti-clockwise rotation of S_H along the Stanovoy foldbelt. Moreover, the transpressive regime in the eastern part of the plate responds to far field plate-boundary forces from the Pacific plate subducting at the Kuril trench and northern Japan.

We show that the FMTI has a high potential for the determination of earthquake focal mechanisms for regions with low seismicity. Hence, it can help to improve the knowledge of the regional stress field, especially in regions with only few stress indicators available.

7 Acknowledgements

We thank two anonymous reviewers for their constructive and detailed remarks. The seismic waveforms were provided by the Broadband Array in Taiwan for Seismology, the China Digital Seismic Network, GEOSCOPE, the Global Seismograph Network (GSN), the Kazakh Network (IGR, NNC), the New China Digital Seismic Network, and the Ocean Hemisphere Network (part of Pacific21). All these data were ordered on-line via the IRIS datacenter Washington (http://www.iris.edu/SeismiQuery). Seismic data was processed with SeismicHandler (Stammler, 1993). Figures were made using GMT (Wessel and Smith, 1998).

References

Arnold, R., Townend, J., Sep. 2007. A bayesian approach to estimating tectonic stress from seismological data. Geophys. J. Int. 170 (3), 1336–1356.

Arvidsson, R., Ekström, G., 1998. Global CMT analysis of moderate earthquakes, Mw≥4.5, using intermediate-period surface waves. Bull. Seism. Soc. Am. 88 (4), 1003–1013.

Barth, A., 2007. Frequency sensitive moment tensor inversion for light to moderate magnitude earthquakes in eastern Africa and derivation of the regional stress field. Ph.D. thesis, University of Karlsruhe.

Barth, A., Reinecker, J., Heidbach, O., 2008. Stress derivation from earthquake focal mechanisms. Tech. rep., World Stress Map Project (http://www.world-stress-map.org).

Barth, A., Wenzel, F., Giardini, D., 2007. Frequency sensitive moment tensor inversion for light to moderate magnitude earthquakes in eastern Africa. Geophys. Res. Lett. 34, L15302.

Bird, P., 2003. An updated digital model of plate boundaries. Geochem. Geophy. Geosy. 4, 1027.

Bott, M. H. P., Mar. 1959. The mechanics of oblique slip faulting. Geol. Mag. 96 (2), 109–117.

Calais, E., Vergnolle, M., San'kov, V., Lukhnev, A., Miroshnitchenko, A., Amarjargal, S., Déverchère, J., Oct. 2003. GPS measurements of crustal deformation in the Baikal-Mongolia area (1994-2002): Implications for current kinematics of asia. J. Geophys. Res. 108 (B10), 2501.

Delvaux, D., Barth, A., submitted. Present-day stress field along the East-African Rift System and implications on the rift dynamics. Tectonophysics.

Delvaux, D., Moeys, R., Stapel, G., Petit, C., Levi, K., Miroshnichenko, A., Ruzhich, V., San'kov, V., 1997. Paleostress reconstructions and geodynamics of the Baikal region, central Asia, part 2. cenozoic rifting. Tectonophysics 282 (1-4), 1–38.

Delvaux, D., Sperner, B., 2003. New insights into structural interpretation and modelling. Vol. 212. Geological Society, London, Ch. New aspects of tectonic stress inversion with reference to the TENSOR program, pp. 75–100.

Doser, D. I., 1991a. Faulting within the western Baikal Rift as characterized by earthquake studies. Tectonophysics 196 (1-2), 87–107.

Doser, D. I., 1991b. Faulting within the eastern Baikal Rift as characterized by earthquake studies. Tectonophysics 196 (1-2), 109–139.

Dziewonski, A. M., Anderson, D. L., Jun. 1981. Preliminary reference earth model. Phys. Earth Plant. Int. 25 (4), 297–356.

Engdahl, E. R., van der Hilst, R., Buland, R., Jun. 1998. Global teleseismic earthquake relocation with improved travel times and procedures for depth determination. Bull. Seism. Soc. Am. 88 (3), 722–743.

Giardini, D., 1992. Moment tensor inversion from mednet data - large worldwide earthquakes of 1990. Geophys. Res. Lett. 19 (7), 713–716.

Heidbach, O., Tingay, M., Barth, A., Reinecker, J., Kurfeß, D., Müller, B.,

this volume. Global spatial wave-length analysis of the tectonic intraplate stress pattern. Tectonophysics.

Heki, K., Miyazaki, S., Takahashi, H., Kasahara, M., Kimata, F., Miura, S., Vasilenko, N. F., Ivashchenko, A., An, K.-D., 1999. The Amurian Plate motion and current plate kinematics in eastern Asia. J. Geophys. Res. 104, 29147–29156.

Henry, C., Woodhouse, J. H., Das, S., 2002. Stability of earthquake moment tensor inversions: Effect of the double-couple constraint. Tectonophysics 356 (1-3), 115–124.

Kreemer, C., Holt, W. E., Haines, A. J., 2003. An integrated global model of present-day plate motions and plate boundary deformation. Geophys. J. Int. 154 (1), 8–34.

Kuge, K., Lay, T., 1994. Data-dependent non-double-couple components of shallow earthquake source mechanisms: Effects of wave-form inversion instability. Geophys. Res. Lett. 21 (1), 9–12.

Larson, E. W. F., Ekström, G., Aug. 2001. Global models of surface wave group velocity. Pure Appl. Geophys. V158 (8), 1377–1399.

Lund, B., Townend, J., Sep. 2007. Calculating horizontal stress orientations with full or partial knowledge of the tectonic stress tensor. Geophys. J. Int. 170 (3), 1328–1335.

McKenzie, D. P., 1969. The relation between fault plane solutions for earthquakes and the directions of the principal stress. Bull. Seism. Soc. Am. 59 (2), 591–601.

Michael, A. J., 1984. Determination of stress from slip data: Faults and folds. J. Geophys. Res. 89 (B13), 11,517–11,526.

Michael, A. J., 1987. Use of focal mechanisms to determine stress: A control study. J. Geophys. Res. 92 (B1), 357–368.

Michael, A. J., Apr. 1991. Spatial variations in stress within the 1987 whittier narrows, california, aftershock sequence - new techniques and results. J. Geophys. Res. 96 (B4), 6303–6319.

Parfenov, L. M., Koz'min, B. M., Imaev, V. S., Savostin, L. A., 1987. Tectonics of the Olekma-Stanovoy seismic belt. Geotectonika 6, 94–108.

Petit, C., Fournier, M., Jan. 2005. Present-day velocity and stress fields of the Amurian plate from thin-shell finite-element modelling. Geophys. J. Int. 160 (1), 358–370.

Radziminovich, N. A., Melnikova, V. I., Miroshnitchenko, A. I., Adyaa, M., Ankhtsetseg, D., Selenge, L., Bayar, G., Tatomir, N. V., this volume. Seismicity and focal solutions of the northern Mongolia and southern Baikal region. Tectonophysics.

Sella, G. F., Dixon, T. H., Mao, A. L., Apr. 2002. Revel: A model for recent plate velocities from space geodesy. J. Geophys. Res. 107 (B4), 2081.

Şengör, A. M. C., Natal'in, B. A., 1996. The tectonic evolution of Asia. Cambridge University Press, Ch. Paleotectonics of Asia: fragments of a synthesis, pp. 486–640.

Stammler, K., 1993. SeismicHandler: Programmable multichannel data han-

dler for interactive and automatic processing of seismological analyses. Comp. Geosci. 19, 135–140.

Šílený, J., 2004. Regional moment tensor uncertainty due to mismodeling of the crust. Tectonophysics 383, 133–147.

Townend, J., Zoback, M. D., Mar. 2006. Stress, strain, and mountain building in central Japan. J. Geophys. Res. 111 (B3), B03411.

Walsh, D., Arnold, R., Townend, J., 2009. A bayesian approach to determining and parametrizing earthquake focal mechanisms. Geophys. J. Int. 176 (1), 235–255.

Wang, Q., Zhang, P. Z., Freymueller, J. T., Bilham, R., Larson, K. M., Lai, X., You, X. Z., Niu, Z. J., Wu, J. C., Li, Y. X., Liu, J. N., Yang, Z. Q., Chen, Q. Z., Oct. 2001. Present-day crustal deformation in China constrained by global positioning system measurements. Science 294 (5542), 574–577.

Wang, S., Xu, Z., 1986. Seismo-tectonic stress field in east China deduced from microearthquakes. In: Reilly, W. I., Harford, B. E. (Eds.), Recent crustal movements of the Pacific region. Vol. 24 of Bulletin of the Royal Society of New Zealand International Lithosphere Program. Publication no. 0102. Royal Society of New Zealand, Wellington, pp. 111–129.

Wei, D.-P., Seno, T., 1998. Determination of the amurian plate motion, in mantle dynamics and plate interactions in east Asia. In: Flower, M., Chung, S.-L., Lo, C.-H., Lee, T.-Y. (Eds.), AGU Geodynamics Series. Vol. 27. American Geophysical Union, Washington, DC, p. pp 419.

Wessel, P., Smith, W. H. F., 1998. New, improved version of Generic Mapping Tools released. Eos, Trans. AGU 79, 579pp.

Woodhouse, J. H., 1988. The calculation of eigenfrequencies and eigenfunctions of the free oscillations of the earth and the sun. In: Doornbos, D. J. (Ed.), Seismological Algorithms. Academic Press, London, pp. 321–370.

Xu, Z.-h., Sep. 2001. A present-day tectonic stress map for eastern Asia region. Acta Seismologica Sinica 14 (5), 524–533.

Xu, Z. H., Wang, S. Y., Huang, Y. R., Gao, A., 1992. Tectonic stress field of china inferred from a large number of small earthquakes. J. Geophys. Res. 97 (B8), 11,867–11,877.

Zheng, Z.-h., Chen, Y.-s., May 2006. A tectonic stress map of China and adjacent regions from earthquakes occurred during 2000–2004. Acta Seismologica Sinica 19 (3), 344–349.

Zoback, M. L., 1992. Stress field constraints on intraplate seismicity in eastern North America. J. Geophys. Res. 97, 11761–11782.

Zonenshain, L., Savostin, L., Jun. 1981. Geodynamics of the Baikal rift zone and plate tectonics of Asia. Tectonophysics 76 (1-2), 1–45.